



HAL
open science

A comprehensive theory for 1-D (an)elastic medium deformation due to plane-wave fluid pressure perturbation

Zongbo Xu, Philippe Lognonné

► **To cite this version:**

Zongbo Xu, Philippe Lognonné. A comprehensive theory for 1-D (an)elastic medium deformation due to plane-wave fluid pressure perturbation. *Geophysical Journal International*, 2024, 236 (3), pp.1499-1512. 10.1093/gji/ggae005 . hal-04398870

HAL Id: hal-04398870

<https://hal.science/hal-04398870>

Submitted on 16 Jan 2024

HAL is a multi-disciplinary open access archive for the deposit and dissemination of scientific research documents, whether they are published or not. The documents may come from teaching and research institutions in France or abroad, or from public or private research centers.

L'archive ouverte pluridisciplinaire **HAL**, est destinée au dépôt et à la diffusion de documents scientifiques de niveau recherche, publiés ou non, émanant des établissements d'enseignement et de recherche français ou étrangers, des laboratoires publics ou privés.



Distributed under a Creative Commons Attribution 4.0 International License

A comprehensive theory for 1-D (an)elastic medium deformation due to plane-wave fluid pressure perturbation

Zongbo Xu¹ and Philippe Lognonné

Université Paris Cité, Institut de physique du globe de Paris, CNRS, F-75005 Paris, France. E-mail: zongboxu@ipgp.fr, zongboxu@u.boisestate.edu

Accepted 2024 January 3. Received 2024 January 1; in original form 2023 September 14

SUMMARY

Atmospheric and oceanic pressure perturbations deform the ground surface and the seafloor, respectively. This mechanical deformation, where the fluid perturbations propagate as plane waves, occurs not only on Earth but also on other planets/bodies with atmospheres, such as Mars, Titan and Venus. Studying this type of deformation improves our understanding of the mechanical interaction between the fluid layer (atmosphere/ocean) and the underlying solid planet/body, and aids investigation of subsurface structures. In this study, we utilize eigenfunction theory to unify existing theories for modelling this deformation and to comprehensively demonstrate possible scenarios of this deformation in homogeneous and 1-D elastic media, including static loading, air-coupled Rayleigh waves and leaky-mode surface waves. Our computations quantitatively reveal that the deformation amplitude generally decays with depth and that reducing seismic noise due to Martian atmosphere requires deploying seismometers at least 1 m beneath Martian surface. We also apply our theory to illustrate how this deformation and the corresponding air-to-solid energy conversion vary on different planetary bodies. Finally, we discuss how medium anelasticity and other factors affect this deformation.

Key words: Planetary seismology; Surface waves and free oscillations; Theoretical seismology; Wave propagation; Seismoacoustics.

1 INTRODUCTION

A fluid layer (e.g. atmosphere or ocean) loads on and interacts with the underlying solid Earth/planet. This interaction can be physical, chemical, or biological. Understanding these diverse types of interactions is one of the ultimate goals of Earth and planetary science. In the physical interaction regime, on which this paper concentrates, fluid pressure perturbations can move and form a local plane wave structure, thus deforming the solid medium surface, such as the ground surface or seafloor. For more complexly structured perturbations, the time-dependent pressure field can always be decomposed as a superposition of plane waves. Therefore, the plane wave approach can also be extended based on such spectral decomposition.

This mechanical deformation has been observed on Earth and was described in the pioneering work of Sorrells (1971). This deformation has also been predicted as a major source of environmental seismic noise on Mars (Lognonné & Mosser 1993), before being observed by the InSight mission (Banerdt *et al.* 2020; Lognonné *et al.* 2020). On these two planets, the fluid pressure perturbations can be generated by atmospheric vortices and infrasound. Seismic signatures of these atmospheric phenomena have been documented (e.g. Langston 2004; Lorenz *et al.* 2015; Lognonné *et al.* 2020; Garcia *et al.* 2022; Onodera *et al.* 2023). Besides of these atmospheric pressure perturbations, oceanic pressure perturbations (i.e.

ocean wave) on Earth also cause deformation of the seafloor (e.g. Longuet-Higgins 1950; Hasselmann 1963).

This mechanical deformation, along with other seismic phenomena like quakes, can be recorded by seismometers on the solid medium surface (i.e. the ground surface or seafloor). The signature of this deformation in the seismic recordings can be modelled and mitigated, based on understanding of this mechanical interaction (e.g. Webb & Crawford 2010; Garcia *et al.* 2020, respectively for Earth's seafloor and Martian surface). This deformation signature can also be utilized to investigate the subsurface structure of terrestrial and extraterrestrial environments (e.g. Crawford *et al.* 1991; Tanimoto & Wang 2019; Lognonné *et al.* 2020, respectively, for Earth's seafloor, Earth's ground surface and Martian surface). In studying this deformation, one commonly uses the ratio between the surface deformation (i.e. recorded by seismometers) and the pressure perturbation (e.g. from meteorological or ocean-bottom observations). This ratio is referred to as *compliance*. In ocean bottom seismic studies, compliance is sometimes called transfer function (e.g. Crawford *et al.* 1991).

There are mainly two types of analytical theories for computing compliance: one for acoustic-wave incidence (e.g. Ben-Menahem & Singh 2012) and the other for fluid moving along the fluid–solid interface (e.g. Yamamoto & Torii 1986; Tanimoto & Wang 2019). In the latter case, when the fluid perturbation moving speed is significantly lower than the seismic-wave velocities of the underlying

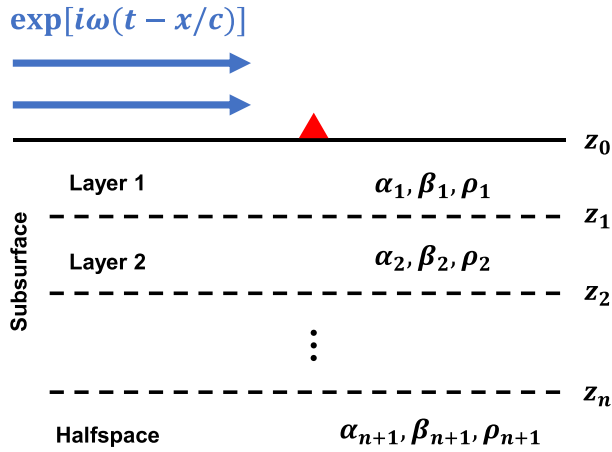


Figure 1. Illustration of the fluid pressure perturbation interacting with the underlying solid medium. The blue arrows represent a moving horizontal pressure field, which can be generated by either acoustic waves (Section 2) or horizontal-moving fluid waves, such as winds or ocean waves (Sections 3 and 4). For the subsurface, a homogeneous medium implies that $n = 0$ (Section 2), while a 1-D medium implies that n is a positive integer (Sections 3 and 4). The red triangle represents a seismometer on the medium surface.

solid medium, another theory has been developed (i.e. Sorrells's theory, Sorrells 1971) to approximate this solid deformation, referred to as static loading. In this study, we demonstrate that utilization of eigenfunction theory is applicable for modelling deformations caused by all these types of fluid perturbations. We also present that our theory can be simplified to Sorrells's theory in case of low-speed perturbations. For acoustic waves, our computation results (i.e. compliance values) are consistent with using the acoustic-wave incidence theory. Note that our theory is similar to existing compliance computation theories (e.g. Crawford *et al.* 1991; Tanimoto & Wang 2019). However, based on our knowledge, it is the first time that one theory is utilized to comprehensively present the deformation scenarios of laterally homogeneous (i.e. 1-D) isotropic elastic media (Section 3).

The existing compliance computations typically focus on the solid medium surface deformation. Indeed, during deformation, the subsurface is also deformed and this deformation amplitude generally decreases with increasing depth. Thus, to reduce this deformation/noise caused by fluid pressure perturbations, seismometers are often buried in land (e.g. Withers *et al.* 1996; Farrell *et al.* 2018) or on the seafloor (e.g. Webb 1998). However, variation of this deformation with depth has rarely been studied theoretically (Sorrells *et al.* 1971; Arai & Tokimatsu 2004). Therefore, in this study, we present computation of compliance at depth using our theory (Section 4). We compute the compliance varying with depth at InSight landing site (Section 5.1). We also apply our theory to various planetary bodies to illustrate compliance variation (Section 5.2). Finally, we discuss how the attenuation of solid media affects compliance and application of compliance to practice (Section 6).

2 COMPLIANCE OF HOMOGENEOUS ELASTIC MEDIA

In this section, we illustrate our computation of compliance of elastic homogeneous media, basis of our 1-D medium compliance computation (Fig. 1 and Section 3). We assume an acoustic-wave or a pressure field which generates surface pressure and displacement

fields proportional to $\exp[i\omega(t - \frac{x}{c})]$, where i denotes the imaginary unit, ω is the angular frequency, t is the propagation time, c is the horizontal apparent velocity and x and z represent the horizontal and vertical axes, respectively. We adopt the zero-shear-stress boundary condition for the medium surface, with continuity of both vertical displacement and vertical stresses/pressure.

2.1 Theory

We define an eigenfunction vector (\vec{f}) to describe the particle motion and stress at a depth (z) in a homogeneous medium following Aki & Richards (2002):

$$\vec{f}(\omega, z) = \begin{bmatrix} U_x \\ U_z \\ T_{zx} \\ T_{zz} \end{bmatrix}, \quad (1)$$

where U_x and U_z represent the horizontal and vertical particle displacement amplitudes, respectively; T_{zx} and T_{zz} are the shear and normal stress amplitudes, respectively. For example, we can write full expressions for the horizontal and vertical particle displacements as the real parts of $iU_x(\omega, z) \exp[i\omega(t - \frac{x}{c})]$ and $U_z(\omega, z) \exp[i\omega(t - \frac{x}{c})]$, respectively.

To solve the particle motions generated by the surface pressure field, we utilize two eigenfunction vectors of homogeneous media: one for downgoing compression (P) waves,

$${}_P\vec{f} = \frac{\exp(-\gamma z)}{\omega} \begin{bmatrix} \alpha\omega/c \\ \alpha\gamma \\ -2\alpha\mu\omega\gamma/c \\ -\alpha\mu(\omega^2/c^2 + v^2) \end{bmatrix}, \quad (2)$$

and the other for downgoing shear (S) waves,

$${}_S\vec{f} = \frac{\exp(-vz)}{\omega} \begin{bmatrix} \beta v \\ \beta\omega/c \\ -\beta\mu(\omega^2/c^2 + v^2) \\ -2\beta\mu\omega v/c \end{bmatrix}, \quad (3)$$

where α and β represent the P - and S -wave velocities of the medium, respectively; $\gamma = \omega\sqrt{1/c^2 - 1/\alpha^2} = i\omega \cos\theta_P/\alpha$ and $v = \omega\sqrt{1/c^2 - 1/\beta^2} = i\omega \cos\theta_S/\beta$ (Aki & Richards 2002, Chapter 7.2). Note that if γ (P waves) or v (S waves) is imaginary-valued, this indicates a homogeneous wave propagating to infinity depth (e.g. scenario a, Section 2.2). For real-valued γ and v , these body waves become inhomogeneous (evanescent) waves, with amplitudes concentrated near the medium surface (e.g. scenario c, Section 2.2).

The total wavefield, a combination of these P and S waves, needs to meet the zero-shear-stress condition on the medium surface (z_0). Therefore:

$$\begin{aligned} \vec{f}(z_0) &= {}_P\vec{f}(z_0) - \frac{{}_P T_{zx}(z_0)}{{}_S T_{zx}(z_0)} {}_S\vec{f}(z_0) \\ &= \begin{bmatrix} \alpha\omega(2\omega^2/c^2 - \omega^2/\beta^2 - 2\gamma v)/c \\ -\alpha\omega^2\gamma/\beta^2 \\ 0 \\ -\alpha\mu\omega^4[(2/c^2 - 1/\beta^2)^2 - 4\gamma v/\omega^2/c^2] \end{bmatrix}. \end{aligned} \quad (4)$$

In this study, we define compliance as the ratio of the horizontal and vertical particle velocities over the atmospheric pressure on

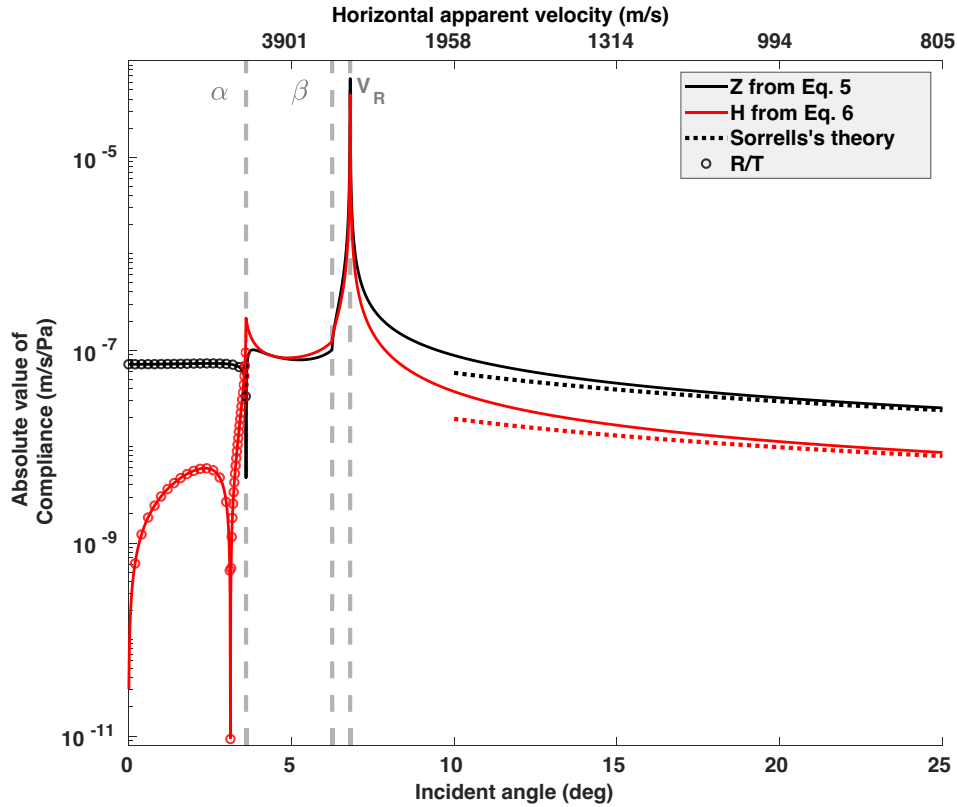


Figure 2. The vertical (black) and horizontal (red) compliance at a solid medium surface due to acoustic-wave incidence under different incident angles (θ in Fig. A1). We convert each incident angle to the corresponding horizontal apparent velocity (c , top x -axis). The solid curves are from our theory, eqs (5) and (6), at a frequency of 1 Hz. The dashed curves between 10° and 25° are from Sorrells's theory (Sorrells 1971). The circles are from the P - S_v -wave reflection and transmission on the air–solid interface (R/T, Appendix A); we stop plotting circles when the incident angle exceeds the critical angle. The elastic properties of this solid medium are following: $\alpha = 5400 \text{ m s}^{-1}$, $\beta = 3120 \text{ m s}^{-1}$ and $\rho = 2600 \text{ kg m}^{-3}$. V_R denotes Rayleigh-wave phase velocity, which is 2868 m s^{-1} in this medium. The acoustic-wave velocity (V_a) is 340 m s^{-1} , typical for Earth atmosphere.

the medium surface, $-T_{zz}(z_0)$. The negative sign accounts for the opposite directions defined as positive for atmosphere pressure and solid normal stress (e.g. Xu *et al.* 2022). Thus, the compliance equations are written as:

$$C_Z(z_0) = \frac{i\omega U_z(z_0)}{-T_{zz}(z_0)} = \frac{-i\gamma}{\mu\omega\beta^2 \left[(2/c^2 - 1/\beta^2)^2 - 4\gamma v/\omega^2/c^2 \right]}, \quad (5)$$

$$C_H(z_0) = \frac{-\omega U_x(z_0)}{-T_{zz}(z_0)} = \frac{-(2\omega^2/c^2 - \omega^2/\beta^2 - 2\gamma v)/c}{\mu\omega^2 \left[(2/c^2 - 1/\beta^2)^2 - 4\gamma v/\omega^2/c^2 \right]}. \quad (6)$$

Note that these two compliance equations are independent of frequency, since ω is cancelled based on the definitions of γ and v . This frequency independence only exists for homogeneous media and is no long valid for 1-D media (Section 3). Furthermore, even in homogeneous media, the particle velocities at depth still vary with frequency, as indicated by $\exp(-\gamma z)$ and $\exp(-vz)$ (eq. S1). Both horizontal and vertical compliance depend on the horizontal apparent velocity (c), which we demonstrate in the following example. Note that in practice, horizontal components also record tilt which is usually dominant at very low frequency ($<0.1 \text{ Hz}$, e.g. Sorrells 1971; Tanimoto & Wang 2019; Garcia *et al.* 2020).

2.2 A Numerical example

We illustrate variation of compliance with different horizontal apparent velocities (Fig. 2). For acoustic waves with velocity V_a , this

variation is related to the acoustic wave incidence, because $c = V_a/\sin\theta$, where θ is the angle between the incidence and vertical direction (Fig. A1). Note that for an acoustic wave propagating in an advecting fluid (like in wind), the horizontal apparent velocity is the sum of $V_a/\sin\theta$ and the advection speed (e.g. Assink 2012), also called effective velocity.

(a) When the horizontal apparent velocity (c) is larger than the P -wave velocity of the solid medium (i.e. $c > \alpha$), the compliance values from eqs (5) and (6) align with those from using the body-wave reflection and transmission coefficient on the medium surface (Appendix A). Such conditions are valid, for example on Mars, where the sound speed in the atmosphere ($\sim 240 \text{ m s}^{-1}$) is significantly higher than the P -wave velocity in the upper layers of the regolith ($\sim 120 \text{ m s}^{-1}$, Lognonné *et al.* 2020; Brinkman *et al.* 2022). On Earth, in marine seismic surveys, small incident angle (nearly vertical) acoustic waves propagate to the ocean bottom (e.g. Hynman & Spence 1992), where this horizontal apparent velocity is larger than the seismic wave velocities in marine sediments.

In these examples ($c > \alpha$), the incident acoustic wave is transmitted into P and S_v waves in the solid medium. The drop in the horizontal compliance (at $\sim 4.1^\circ$ in Fig. 2) is due to the amplitude cancellation between the P and S_v waves. When $c = \alpha$, the P wave propagates horizontally along the solid medium surface. This leads to predominantly horizontal ground motion, therefore a peak in the horizontal compliance values and a trough in the vertical compliance values ($c = \alpha$ in Fig. 2).

(b) When the horizontal apparent velocity is lower than the P -wave velocity (i.e. $c < \alpha$), the transmitted P waves become inhomogeneous waves. Inhomogeneous waves propagate along the solid medium surface, and their amplitude decays with depth (e.g. Aki & Richards 2002, Chapter 5.3). Furthermore, if $c > \beta$, a common condition for ocean-bottom seismometers installed on water-rich sediments (e.g. Schumann *et al.* 2014), the transmitted S waves are still homogeneous waves. In contrast, if $c < \beta$, typically the case for seismometers deployed on bedrocks on Earth with respect to infrasound, the S waves also become inhomogeneous waves. Therefore, we observe a dramatic change in the compliance value trends at $c = \beta$ (Fig. 2).

Note that, when c is equal to the Rayleigh-wave phase velocity (V_R) of the solid medium, both the vertical and horizontal compliance values reach their maxima (Fig. 2), because based on Aki & Richards (2002),

$$\left(\frac{2}{c^2} - \frac{1}{\beta^2}\right)^2 - 4\frac{\gamma\nu}{\omega^2 c^2} \quad (7)$$

$$= \left(\frac{1}{\beta^2} - 2p^2\right)^2 + 4p^2 \frac{\cos(\theta_P)\cos(\theta_S)}{\alpha\beta}, \quad (8)$$

$$= 0, \quad (9)$$

where $p = 1/c$ and is called ray parameter, and thus the denominators of eqs (5) and (6) become zeros. Therefore, a Rayleigh wave is activated by this incidence, and both the vertical and horizontal compliance peak values occur ($c = V_R$ in Fig. 2). This Rayleigh wave is normally referred to as air-coupled Rayleigh wave (e.g. Ewing *et al.* 1957).

(c) When the horizontal apparent velocity is significantly lower than the S -wave velocity (i.e. $c \ll \beta$), both the transmitted P and S waves become inhomogeneous waves. This scenario occurs in cases of deformations generated by winds on Earth and Mars, or by ocean waves loading on Earth's ocean bottom. The compliance equations (eqs 5 and 6) can be theoretically simplified to Sorrells's theory (Sorrells 1971) after the elimination of the $(c/\beta)^2$ terms (Appendix B). The compliance values from Sorrells's theory agree well with our theory when c is lower than 1000 m s^{-1} , approximately $\frac{1}{3}\beta$ (Fig. 2). This scenario is referred to as static loading.

We note that compliance computations similar to ours have previously been conducted using the P - S_V -wave reflection and transmission at the fluid-solid interface (e.g. Edwards *et al.* 2008; Stutzmann *et al.* 2021). This reflection and transmission method is referred to as R/T method in the following. R/T method is theoretically equivalent to ours (e.g. Aki & Richards 2002, Chapter 7). Therefore, these two methods generate identical compliance values (Fig. 2). Note that our method can deal with not only atmospheric/oceanic acoustic waves but also winds and ocean waves, while R/T method is primarily developed for acoustic waves. R/T method also requires determining incidence/reflection angles and consequently particle motion rotation, which are not needed in our computations. Furthermore, our method in this section is the basis for computing compliance of a 1-D solid medium in the next section.

3 COMPLIANCE OF 1-D ELASTIC MEDIA

3.1 Theory

We calculate the compliance of a 1-D medium (Fig. 1) utilizing the eigenfunction vector in Section 2. We adopt the propagation matrix

method (e.g. Aki & Richards 2002, Chapter 7.2.2) to solve for the vector at different depths. For example, if we have \vec{f} at one depth (z) in a layer and the propagation matrix of this layer (\mathbf{P}), we can compute \vec{f} at any depth (z') within this layer as:

$$\vec{f}(z') = \mathbf{P}(z' - z)\vec{f}(z), \quad (10)$$

where the formula for each element in \mathbf{P} is in Aki & Richards (2002). At the interface between two solid layers, \vec{f} should be continuous from the lower to the upper layers; otherwise these two layers would be split during elastic deformation. Therefore, we write \vec{f} at the solid medium surface as

$$\vec{f}(z_0) = \prod_{m=1}^n \mathbf{P}_m(z_{m-1} - z_m)\vec{f}(z_n), \quad (11)$$

where $\vec{f}(z_n)$ is the eigenfunction vector on the top of the half-space (Fig. 1). Note that there is another way to compute the eigenfunction at the medium surface, numerical integration (e.g. Aki & Richards 2002, Chapter 7.2.1), adopted by Tanimoto & Wang (2019).

By applying the propagation matrix method to the P - and S -wave eigenfunction vectors (${}_P\vec{f}$ and ${}_S\vec{f}$) of the homogeneous media (i.e. the half-space, eqs 2 and 3), we determine the eigenfunction vectors at the solid medium surface (z_0) as:

$${}_P\vec{f}(z_0) = \prod_{m=1}^n \mathbf{P}_m(z_{m-1} - z_m){}_P\vec{f}(z_n), \quad (12)$$

$${}_S\vec{f}(z_0) = \prod_{m=1}^n \mathbf{P}_m(z_{m-1} - z_m){}_S\vec{f}(z_n). \quad (13)$$

To satisfy the zero-shear-stress boundary condition, following the same logic in Section 2, we eliminate the shear-stress term in $\vec{f}(z_0)$:

$$\vec{f}(z_0) = {}_P\vec{f}(z_0) - \frac{{}_P T_{zx}(z_0)}{{}_S T_{zx}(z_0)} {}_S\vec{f}(z_0). \quad (14)$$

We then compute the compliance at the medium surface using eqs (5) and (6). Xu *et al.* (2022) benchmarked our computation against a numerical simulation software, SPECSEM2D-DG (Brisaud *et al.* 2017; Martire *et al.* 2022). We also utilize this software later to benchmark our computation of compliance variation with depth (Appendix C).

3.2 Different compliance scenarios

We comprehensively illustrate deformation scenarios for a fluid pressure perturbation propagating at different horizontal apparent velocities (c) along the surface of a two-layer solid medium (Table 1). This perturbation could be an acoustic-wave incidence (like in Section 2.2) or plane-wave wind/ocean waves (e.g. Sorrells *et al.* 1971; Crawford *et al.* 1991; Tanimoto & Wang 2019). For each horizontal apparent velocity, we compute the compliance in a frequency band (from 0.1 to 5 Hz) and visualize the vertical/horizontal compliance varying with frequency (Figs 3 and S1). Note that different from homogeneous media, the compliance of 1-D media varies with frequency, because different wavelengths sample the medium layers differently (Section 4). We also convert the compliance values from the frequency domain to the time domain. This transformation result can be interpreted as the ground-motion waveform caused by a fluid-pressure-perturbation impulse from 0.1 to 5 Hz (Figs 3 and S1). We present how both the frequency-domain compliance values and the time-domain waveforms vary with respect to four different horizontal apparent velocities in the following:

(a) When the horizontal apparent velocity is higher than the P -wave velocity of the half-space (i.e. $c > \alpha_2$), both the P and S_V waves

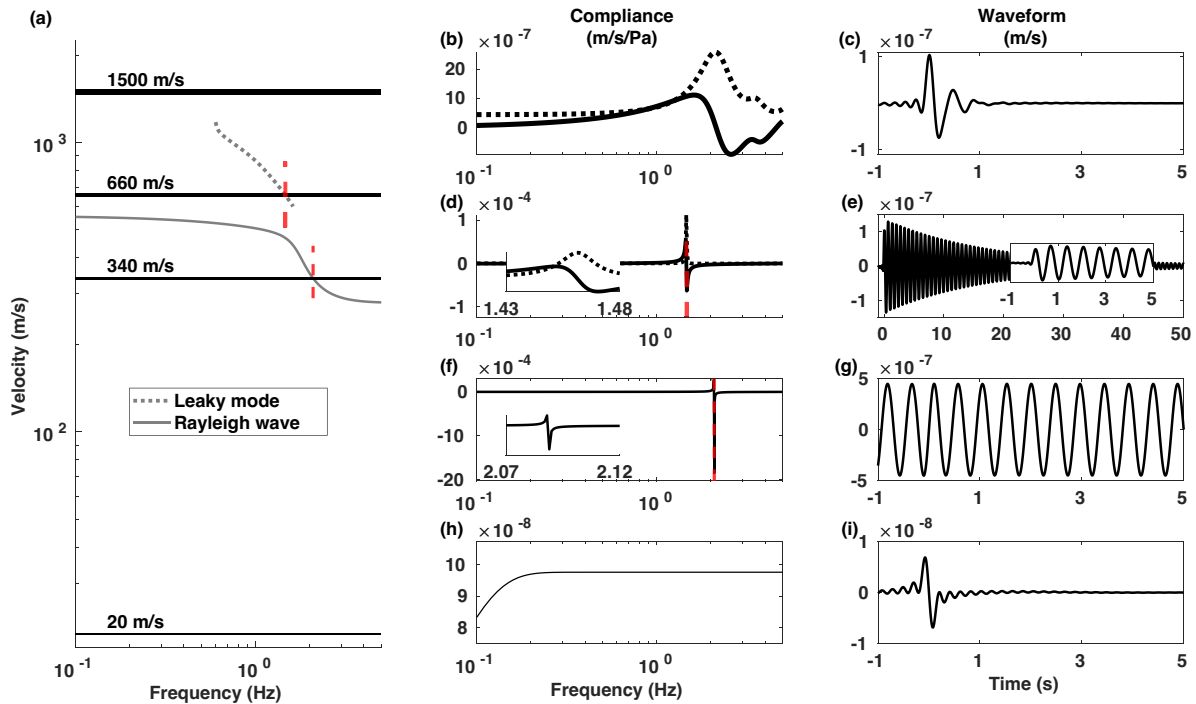


Figure 3. Illustration of the solid medium deformation due to a fluid pressure perturbation with four horizontal apparent velocities (1500, 660, 340 and 20 m s^{-1}), corresponding to the four scenarios in Section 3. For each horizontal apparent velocity, we compute the frequency-domain vertical compliance at the surface (central column). The real and imaginary parts of the compliance are plotted in dashed and solid curves, respectively. We then convert the compliance to the time domain to represent the ground-motion waveform (right-hand column). The elastic parameters of this solid medium are in Table 1. From these parameters, we compute the phase velocities of the Rayleigh wave and the leaky-mode surface wave (a). The same figure for the horizontal compliance is Fig. S1.

from the pressure perturbation propagate as homogeneous waves within the solid medium. These body waves mainly propagate to infinite depth. Thus, the ground motions are transient (Figs 3c and S1c).

This scenario occurs in cases of oblique (nearly vertical) acoustic wave incidence on the surface of an onshore/offshore sedimentary structure. The transmitted body waves are sometime called seismic precursors in air-ground coupling (e.g. Sorrells *et al.* 2002; Edwards *et al.* 2008). In marine seismic surveys, these body waves are utilized to investigate marine geological structures (e.g. Hyndman & Spence 1992).

(b1) When the horizontal apparent velocity is lower than the half-space P -wave velocity but higher than the half-space S -wave velocity (i.e. $\beta_2 < c < \alpha_2$), the P waves in the half-space propagate as inhomogeneous waves. Consequently, the P waves are trapped in the first layer. Meanwhile, S_v waves still propagate as homogeneous waves in the whole solid medium. Therefore, the S_v waves propagating to infinite depth leads to S_v -wave energy leakage. Furthermore, if c is equal to the leaky-mode surface-wave phase velocity (V_L , e.g. Aki & Richards 2002), we observe a pulse occurring in both the vertical and horizontal compliance (Figs 4d and S1d), thus activating a leaky-mode surface wave. This leaky-mode surface-wave amplitude decays over time (Fig. 4e) due to the S_v -wave leakage in the half-space. Note that this leaky-mode surface-wave activation has been reported by Langston (2004), but the author did not explicitly link this activation to V_L .

This type of scenarios commonly occurs in shallow water seismic surveys where the airguns excite acoustic waves in water (e.g. Ritzwoller & Levshin 2002; Boiero *et al.* 2013). Detailed discussion

about leaky-mode surface waves can be found in Gilbert (1964) and Aki & Richards (2002).

(b2) When the horizontal apparent velocity becomes even lower than the half-space S -wave velocity (i.e. $c < \beta_2$), both the P and S_v waves propagate as inhomogeneous waves in the half-space, leading to no energy leakage anymore. Similarly to the homogeneous medium scenario b, an air-coupled Rayleigh wave is activated at the frequency where $c = V_R$. At this specific frequency, the compliance values are approximately two orders of magnitude larger (a factor of 100) than at other frequencies (Fig. 4f and S1f). In the time domain, this activated Rayleigh wave keeps resonating due to the absence of energy leakage. This waveform resembles those observed in field studies, where a monochromatic wave lasts from a few seconds to over 10 s (e.g. Langston 2004; Edwards *et al.* 2007). Note that in our synthetic waveform (Fig. 3g), the Rayleigh wave existing prior to the time zero is due to the periodic nature of the Discrete Fourier Transform. We discuss removing this acausal waveform and damping the waveform in Section 6.1.

These scenarios have been observed through seismometers deployed on sediments overlying bedrocks in response to acoustic sources such as meteors (e.g. Edwards *et al.* 2008), lighting (e.g. Lin & Langston 2007), and airborne human activities (e.g. Edwards *et al.* 2007; Novoselov *et al.* 2020). Note that natural sources (like storms) and artificial acoustic sources (like airguns) in marine seismic surveys activate Rayleigh and Scholte waves, possessing energy in both solid and fluid media (e.g. Ruan *et al.* 2014). Thus, we do not list this activation in Table 2.

(c) When $c \ll \beta_1 < \beta_2$, the compliance values vary smoothly in the frequency domain without any pulse. In the time domain, the ground motion primarily exhibits one main wiggle, while the other

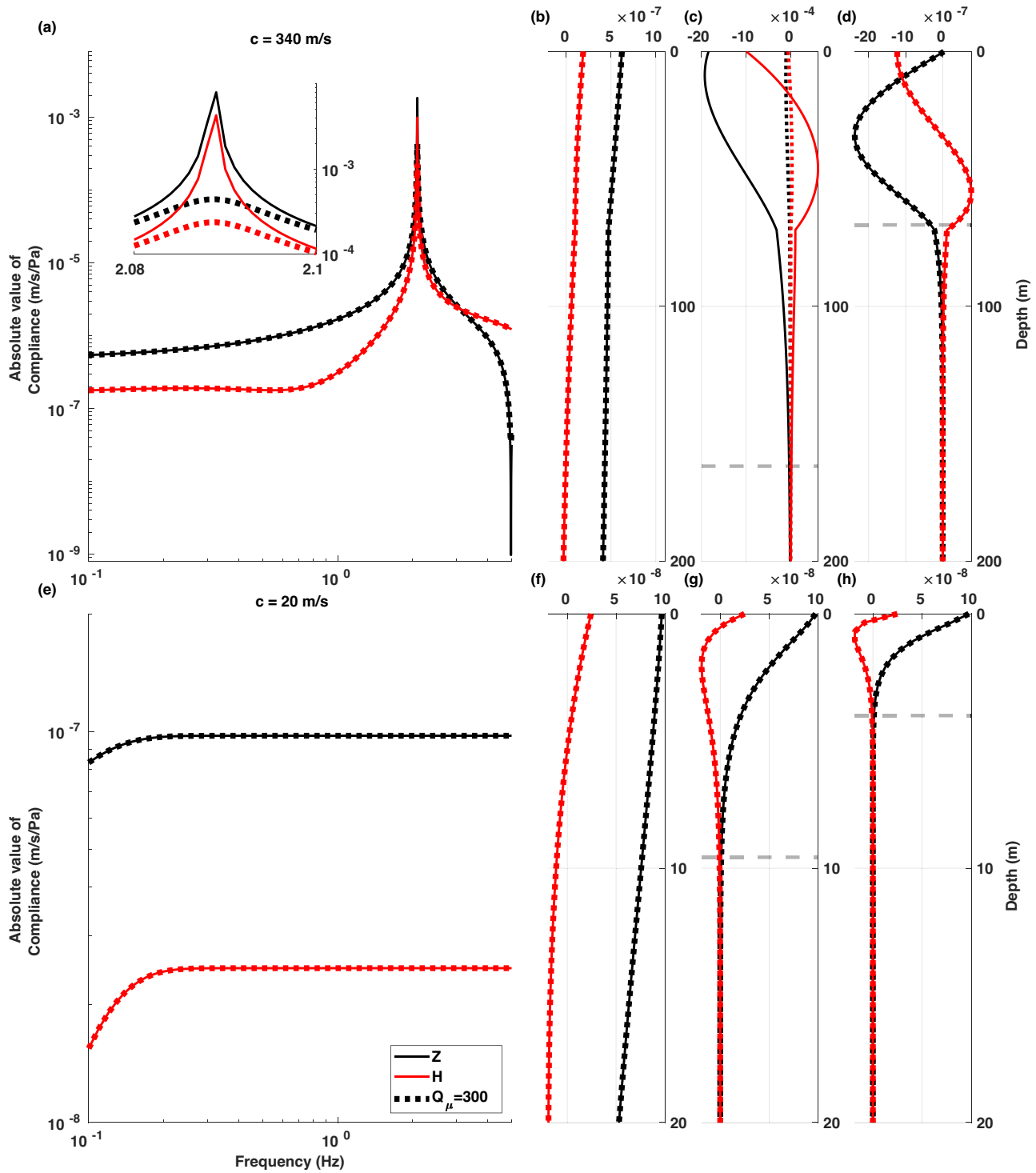


Figure 4. The compliance at (a,e) and beneath (b–d, f–h) the solid medium surface (Table 1). The compliance at depth is computed for frequencies of 0.2 (b, f), 2.09 (c, g) and 5 Hz (d, h). The 2.09 Hz frequency corresponds to the air-coupled Rayleigh-wave activation (inset in a). The black and red curves represent the vertical and horizontal compliance values, respectively. The solid curves are for the elastic medium (Table 1), while the dotted curves are for the same medium with an attenuation factor of $Q_\mu = 300$. The compliance computation of anelastic media is detailed in Section 6.1. The horizontal grey dashed line in each subplot (b–d, f–h) marks the depth equal to one wavelength.

small wiggles are numerical noise. This scenario—static loading—has been observed on Earth’s ground surface due to horizontally propagating infrasound and winds (e.g. Sorrells *et al.* 1971; Ichihara *et al.* 2012; Lorenz *et al.* 2015; Tanimoto & Wang 2019), on Earth’s

seafloor due to ocean waves (e.g. Yamamoto & Torii 1986; Crawford *et al.* 1991) and on Martian surface due to dust devils (e.g. Lognonné *et al.* 2020; Kenda *et al.* 2020; Garcia *et al.* 2020) and guided infrasound (Garcia *et al.* 2022; Xu *et al.* 2022).

Table 1. The two-layer subsurface model parameters used in Sections 3 and 4.

Layer number	V_P (m s ⁻¹)	V_S (m s ⁻¹)	Density (kg m ⁻³)	Thickness (m)
1	596	300	1531	70
2	1191	600	1821	∞

4 COMPLIANCE VARYING WITH DEPTH

In the sections above, we focus on the compliance at the solid medium surface (e.g. the surface of Earth or Mars). Using the same theory in Section 3, we compute the compliance beneath this surface. We define the compliance at a given depth (z) as the ratio of the ground motion at this depth over the fluid-perturbation pressure on the surface (z_0):

$$C_Z(z) = \frac{i\omega U_z(z)}{-T_{zz}(z_0)}, \quad (15)$$

$$C_H(z) = \frac{-\omega U_x(z)}{-T_{zz}(z_0)}, \quad (16)$$

where $T_{zz}(z_0)$ is from $\vec{f}(z_0)$ in Section 3. $U_z(z)$ and $U_x(z)$ are from the eigenfunction vector at the depth, $\vec{f}(z)$, similar to eq. (14):

$$\vec{f}(z) = {}_P \vec{f}(z) - \frac{{}_P T_{zx}(z_0)}{{}_S T_{zx}(z_0)} {}_S \vec{f}(z). \quad (17)$$

We benchmark our computation using eqs (15) and (16) in Appendix C. Our computation is applicable to both homogeneous and 1-D media.

Utilizing the theory above, we compute the compliance at various depths within the same 1-D solid medium as used in the previous section (Table 1). We focus on the compliance scenarios where no body waves leak to infinite depth (i.e. $c < \beta_2$), because these scenarios (b2 and c) activated by natural sources are commonly observed. At a given frequency (f), the compliance amplitude generally decays with increasing depth (Figs 4 and S2). We note that the signs of the vertical and horizontal compliance at the surface can be either the same (Fig. 4b) or opposite (Fig. S2d). This indicates that the phase shift between these two components can be either $\pi/2$ or $3\pi/2$, determined by the frequency and the model of the solid medium.

Compared to at the surface, the compliance value approaches much close to zero when the depth exceeds one wavelength (c/f , Figs 4 and S2). Furthermore, because the half-space in our medium is more rigid than the first layer, the compliance amplitude in the half-space decays faster with depth compared to in the first layer (Figs 4c and d). This observation supports that burying a seismometer reduces the seismic noise due to fluid pressure perturbations (e.g. Webb 1998; Withers *et al.* 1996). We discuss this effect quantitatively in the context of NASA's InSight mission in Section 5.1.

5 APPLICATION OF COMPLIANCE TO PLANETARY SEISMOLOGY

Compliance has been utilized in investigating Earth's/Martian subsurface and in modelling seismic signatures of ocean waves and Martian winds, as stated in Section 1. In this section, we explore two new applications of compliance computation in planetary seismology.

5.1 Noise reduction through burying InSight seismometers

NASA's InSight seismometer module records abundant atmospheric noises, especially during daytime (e.g. Lognonné *et al.* 2020; Banerdt *et al.* 2020). These noises lead to significantly fewer marsquakes detected in the daytime compared to the nighttime (e.g. Giardini *et al.* 2020; Lognonné *et al.* 2023). To reduce these noises, burying seismometers has been demonstrated to be an effective solution on Earth (Withers *et al.* 1996; Farrell *et al.* 2018). Here we focus on the noise caused by the atmospheric pressure perturbations (e.g. Garcia *et al.* 2020) and investigate the theoretical depth for the InSight seismometer module in order to reach a 90 per cent noise reduction compared to on Martian surface.

We apply our computation (Section 4) to a subsurface velocity model of InSight landing site under winds at three different speeds (5, 10 and 20 m s⁻¹). This model, from studying Martian infrasound (Xu *et al.* 2022), consists of a 0.6-m-thick fine-sand regolith layer, a 40-m-thick coarse regolith layer, and a fractured basalt half-space (Table S1). For a given frequency, we compute both vertical and horizontal compliance values at various depths to determine a burying depth where the compliance values are reduced to 10 per cent of the compliance at the surface (Fig. S3). This burying depth increases with decreasing frequency (Fig. 5). At high frequencies (>1 Hz), burying the InSight seismometers beneath the fine-sand regolith is effective for winds at 5 m s⁻¹. However, at higher wind speeds, this burying depth becomes less effective for the noise reduction. At low frequencies (<1 Hz), important for Marsquake data analysis (e.g. Knapmeyer-Endrun *et al.* 2021; Khan *et al.* 2021; Stähler *et al.* 2021), the required burying depth is at least 1 m and can exceed 10 m for even lower frequencies. However, accessing such depths (>1 m) on Mars is challenging for space-mission engineering.

5.2 Air-ground coupling on different planetary bodies

Air-ground coupling occurs on a solid body with an atmosphere. Here we compare compliance on Earth, Venus, Mars and Titan. For comparison, we adopt a homogeneous model of the upper crust of each body (Table 3), and thus the compliance values here represent the lower limit. We note that all the compliance values of these bodies are around 10^{-7} (Fig. 6), except when $c = \alpha$ (the drops) or an air-coupled Rayleigh wave is activated (the peaks). This indicates that a similar pressure perturbation would generate deformations of comparable amplitudes on these bodies, if we do not consider the heterogeneity of the upper crusts. However, due to different atmospheric parameters (e.g. air density) among these bodies, a same atmospheric phenomenon can lead to varying magnitude of pressure on different bodies (e.g. dust devil, Lorenz 2021). Therefore, we instead focus on comparing mechanical energy conversions on these bodies.

We present the energy ratio of acoustic waves converting to seismic waves (Section A), representing energy conversion from air to solid (e.g. Lognonné & Johnson 2007). This conversion is most efficient on Venus, where $\sim 10^{-2}$ of the acoustic-wave energy is converted to the solid. In contrast, on Mars, the conversion ratio is only $\sim 10^{-6}$. These two end-member observations agree well with (Lognonné *et al.* 2016). Meanwhile, our computation suggests that seismic observation of infrasound on Titan ground surface is theoretically possible. The conversion rate on Titan, $\sim 10^{-3}$, is an order of magnitude (a factor of 10) higher than on Earth, while on Earth, this air-to-solid conversion has already been commonly observed

Table 2. Summary of the four coupling scenarios in a two-layer elastic medium (Table 1). α_2 and β_2 are the P - and S -wave velocities of the half-space, respectively. β_1 is the first-layer S -wave velocity. Further details and corresponding references can be found in Section 3.

Velocity relationship	Seismic-wave types in the half-space	Pressure field examples	Observation sites or environments
$c > \alpha_2$	Homogeneous P and S_v waves	Oblique (nearly vertical) acoustic wave incidence generated by meteors or airguns	Onshore seismic stations, marine seismic surveys
$\beta_2 < c < \alpha_2$ ($c = V_L$)	Inhomogeneous P waves Homogeneous S_v waves (leaky-mode surface waves)	Acoustic waves generated by airguns	Shallow water seismic surveys
$c < \beta_2$ ($c = V_R$)	Inhomogeneous P and S_v waves (air-coupled Rayleigh waves)	Infrasound generated by meteors, lighting, airborne human activities	Sedimentary structures
$c \ll \beta_1$	Inhomogeneous P and S_v waves in the both layers	horizontal-propagating infrasound and winds, dust devils, ocean waves	Earth's seafloor, Martian and Earth's surfaces

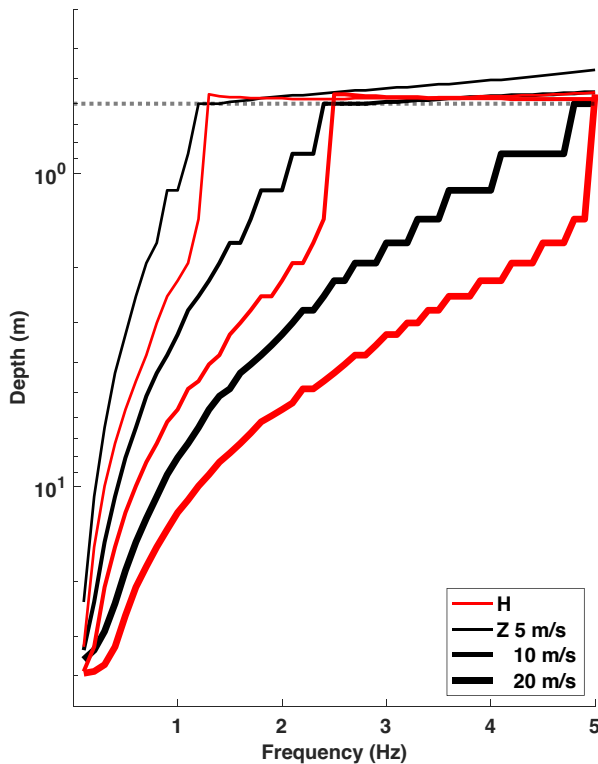


Figure 5. Burying depth of InSight seismometer module under three wind-speed conditions. The red and black curves represent the required burying depths where the horizontal and vertical compliance values, respectively, are reduced to 10 per cent of the ones at the ground surface. Compliance varying with depth at InSight landing site is illustrated in Fig. S3. The dotted grey line indicates the thickness of the surface fine-sand regolith, 0.6 m.

(Table 2). Given that NASA's Dragonfly mission will bring geophones to Titan, it is reasonable that Titan infrasound, if exists, might be observed in seismic data from Dragonfly.

In this section, we focus on the energy conversion from air to solid ground. However, in reality, fully coupled acoustic-Rayleigh waves exist, involving energy conversion both from air to solid and from solid to air. To physically model these waves, we need to adopt other computation tools like in Lognonné *et al.* (1998).

6 DISCUSSION

Our compliance computations above are for elastic media with flat surfaces. However, seismic attenuation and other factors (such as

topography and turbulence) may affect computation and utilization of compliance. Thus, we discuss these factors in this section.

6.1 Damping the synthetic air-couple Rayleigh wave

Our synthetic air-couple Rayleigh wave does not attenuate with propagation time (Fig. 3g), where this type of signal in field observation does possess limited duration. To improve our synthetic waveform, we incorporate attenuation into our solid medium model as

$$\mu^* = \mu + i \frac{\mu}{Q_\mu}, \quad (18)$$

where μ is the shear modulus and Q_μ is the quality factor (e.g. Kramer 2002). By utilizing this complex-valued shear modulus in our compliance computation (Section 3), the compliance around air-coupled Rayleigh-wave activation in the frequency domain becomes smoother compared to the elastic case (Fig. 4a). After transforming this new compliance into the time domain, we observe that the resulting waveform attenuates with time (Figs 7a and b). This new waveform also presents a phase shift compared to the waveform in the elastic case due to the complex-valued shear modulus (Fig. 7a). Meanwhile, we also observe that incorporating this damping does not notably alter the compliance values where no air-coupled Rayleigh wave is activated (Figs 4 and 7). This agrees with our intuition that the attenuation damps the dynamic part of the elastodynamic (i.e. seismic waves), rather than the static part like static loading. This observation is also consistent with fluid mechanics studies (e.g. Benschop *et al.* 2019). Therefore, it is necessary to incorporate attenuation into modelling air-coupled Rayleigh waves, especially at high frequencies.

6.2 Future work and limitation

Our compliance computation is currently based on a flat surface. However, both the ground surfaces and seafloors can have topography. This topography can affect acoustic-wave incidence or ocean-wave horizontal apparent velocity (e.g. Hasselmann 1963; Arduin *et al.* 2015; Bishop *et al.* 2021). Thus, in the future, we need to incorporate this topography into our compliance computation. Through incorporating this factor, we can, for example, apply our compliance computation to estimate ground motion on topographic seafloors under ocean waves. Such estimations will aid mitigation of the ocean-wave effects from the ocean-bottom seismic data recorded by seismometers or distributed acoustic sensing systems.

The fundamental assumption of our study is that the fluid pressure perturbations propagate as plane waves. However, in reality,

Table 3. Near surface air properties and upper-crust velocity models of different bodies. The acoustic-wave velocities and air densities are from (Lognonné & Johnson 2007) and (Petulescu & Achi 2012). The velocity model parameters of Mars and Titan are from (Stähler *et al.* 2021) and (Marusiak *et al.* 2022), respectively. We adopt the velocity model of Earth to describe Venus upper crust, since accurate estimation of Venus upper crust is not available.

Body	V_P (m s ⁻¹)	V_S (m s ⁻¹)	Density (kg m ⁻³)	V_a (m)	Air density (kg m ⁻³)
Earth	5400	3120	2600	340	1.225
Venus	5400	3120	2600	426	65
Mars	3800	1850	2300	214	0.0175
Titan	4100	2100	960	190	5.34

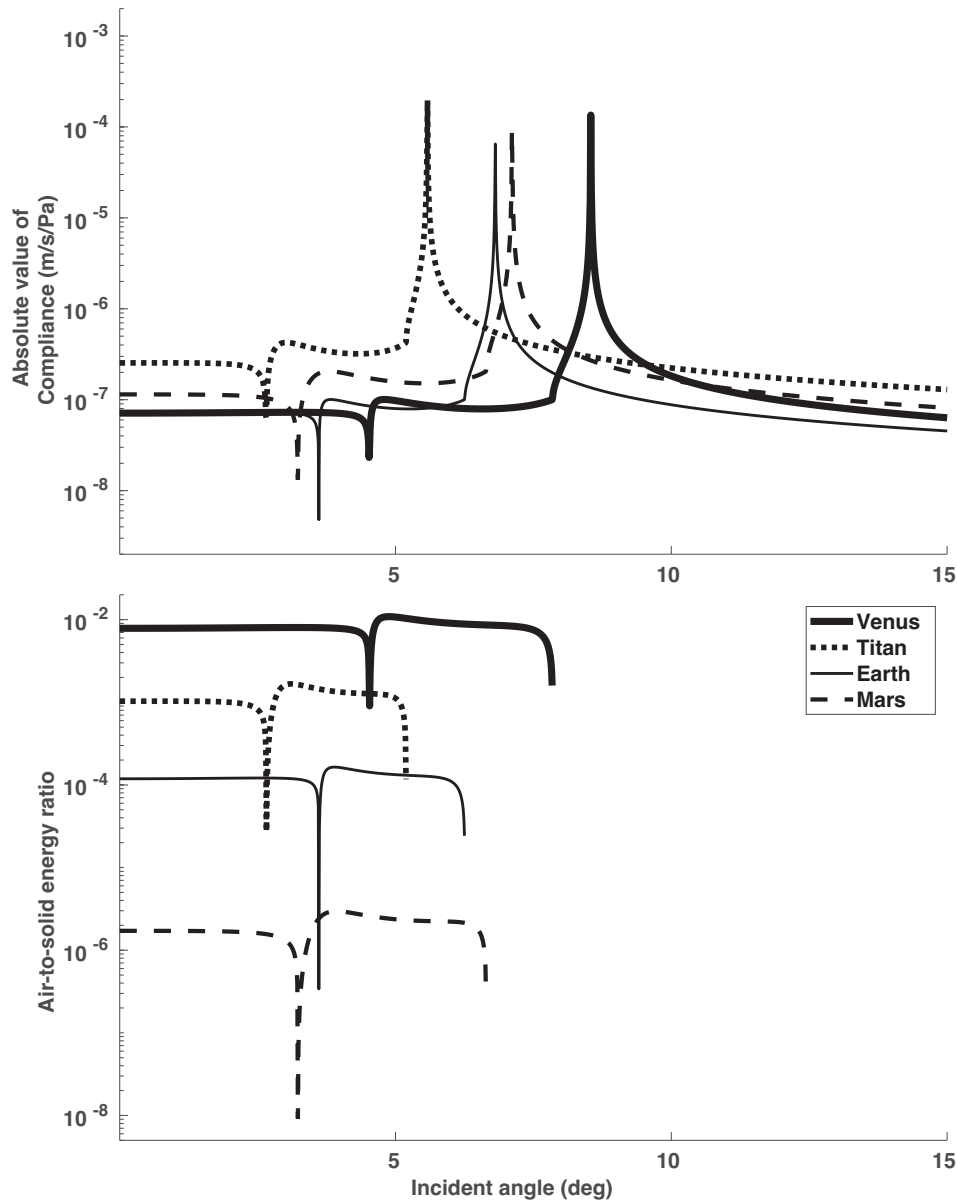


Figure 6. The vertical compliance on different planetary bodies due to acoustic-wave incidence (top panel) and the corresponding air-to-solid energy ratio (bottom panel). The corresponding horizontal compliance is in Fig. S4. The compliance curves of Earth are identical to the ones in Fig. 2. This energy conversion become almost zero when both P and S_V waves become inhomogeneous waves in the solid medium.

fluid can exhibit turbulence and still deform the solid medium surface (e.g. Yu *et al.* 2011). To model this deformation, one solution is decomposing the turbulent pressure field into plane waves and then applying compliance computation to these decomposed plane waves (e.g. Kenda *et al.* 2017). Note that this approach still requires

validation in practice. Meanwhile, wind gust can generate the seismic/mechanical noise by shaking seismometers (e.g. Mucciarelli *et al.* 2005), or the nearby objects such as a tree (e.g. Johnson *et al.* 2019) or a space-mission lander (e.g. Anderson *et al.* 1976; Murdoch *et al.* 2017; Stott *et al.* 2021). Furthermore, a special type of

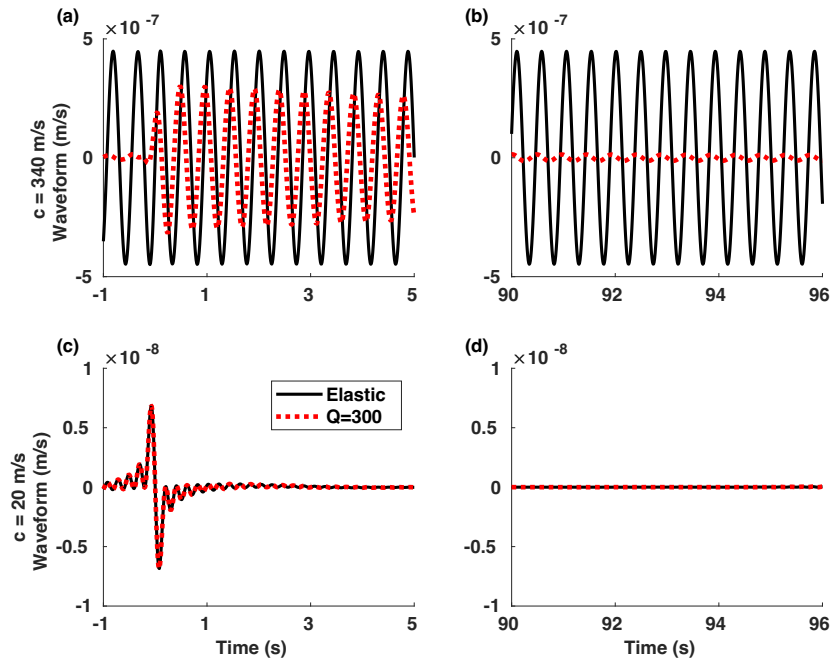


Figure 7. The vertical-component waveforms on the solid medium surface due to a fluid pressure perturbation. The horizontal-apparent velocity is 340 m s^{-1} (top row) or 20 m s^{-1} (bottom row). The x -axis is the propagation time. The solid curves are from the elastic solid medium and the dashed curves are from the anelastic medium with $Q = 300$ (Section 6.1). The waveform computation parameters match those in Fig. 3. The solid curves in a and c are the same as in Figs 3(g) and (i). For completeness, the corresponding horizontal-component waveforms are in Fig. S5.

air-ground interaction, gas leakage from depth, can also generate seismic waves, potentially contaminating field seismic recordings (e.g. Umlauf & Korn 2019; Xu *et al.* 2020). At this point, theoretical tools for modelling these types of shaking or deformation are either missing or still in developing.

To fully model and mitigate all these effects from seismic recordings, we need not only analytical compliance computation, but also the numerical simulations (e.g. Zhang *et al.* 2022) and both the lab and field experiments (e.g. Nishikawa *et al.* 2014; Farrell *et al.* 2018).

7 CONCLUSION

We utilize eigenfunction theory to compute compliance in both homogeneous and laterally homogeneous isotropic elastic media. Our computation provides compliance values at and beneath the medium surface. For homogeneous media, we benchmark our computation against the acoustic-wave reflection and transmission coefficient method and SPECFEM2D-DG. We also demonstrate that our theory is theoretically equivalent to Sorrells's theory when the horizontal apparent velocity is significantly lower than the shear-wave velocity.

Based on our computation, we comprehensively present medium deformation scenarios (e.g. body-wave conversion, leaky-mode surface wave, air-coupled Rayleigh wave, and static loading) generated by fluid pressure perturbations propagating as plane waves. We also quantitatively demonstrate that these medium deformations are mainly concentrated within the one-wavelength depth range. Application of our theory to a subsurface model of InSight landing site suggests that a reduction of 90 per cent of Martian atmospheric noise in seismic recording requires burying InSight seismometers at least 1 m beneath Martian surface. Through comparing compliance on different planetary bodies, we emphasize the potential for

seismic observation of infrasound on Titan. Our research will aid understanding and modelling the mechanical interaction between the solid Earth/planets and the overlying fluid (atmosphere/ocean).

ACKNOWLEDGMENTS

ZX thanks Prof Paul Michaels for his suggestion about coding the propagation-matrix computation in 2017 Fall. ZX also thanks Dylan Mikesell, Eléonore Stutzmann and Ludovic Margerin for fruitful discussions. The authors thank assistant editors, Louise Alexander and Fern Storey, for their coordination in the review process. The authors also thank editor Andrea Morelli and an anonymous reviewer for their positive feedback which helped improve this manuscript.

The authors acknowledge the financial support from CNES, ANR MAGIS (ANR-19-CE31-0008-08), ANR BRUIT-FM (ANR-21-CE01-0031) and the Initiative d'Excellence (IdEx) Université Paris Cité (ANR-18-IDEX-0001).

DATA AVAILABILITY

We use synthetic data and have described how to generate the synthetic data in the manuscript. 1-D medium compliance computation code is available at <https://github.com/ZongboXu/HFGI>. SPECFEM2D-DG is from Martire *et al.* (2022).

SUPPORTING INFORMATION

Supplementary data are available at *GJI* online.

Xu2023_Compliance_SI.pdf

Please note: Oxford University Press is not responsible for the content or functionality of any supporting materials supplied by the

authors. Any queries (other than missing material) should be directed to the corresponding author for the paper.

REFERENCES

- Aki, K. & Richards, P.G., 2002. *Quantitative Seismology*, Science Books.
- Anderson, D.L. *et al.*, 1976. The Viking seismic experiment, *Science*, **194**(4271), 1318–1321.
- Arai, H. & Tokimatsu, K., 2004. S-wave velocity profiling by inversion of microtremor H/V spectrum, *Bull. seism. Soc. Am.*, **94**(1), 53–63.
- Arduhin, F., Gualtieri, L. & Stutzmann, E., 2015. How ocean waves rock the Earth: two mechanisms explain microseisms with periods 3 to 300 s, *Geophys. Res. Lett.*, **42**(3), 765–772.
- Assink, J.D., 2012. *Infrasound as upper atmospheric monitor*, PhD thesis, University of Mississippi.
- Banerdt, W.B. *et al.*, 2020. Initial results from the InSight mission on Mars, *Nat. Geosci.*, **13**(3), 183–189.
- Ben-Menahem, A. & Singh, S.J., 2012. *Seismic Waves and Sources*, Springer Science & Business Media.
- Benschop, H., Greidanus, A., Delfos, R., Westerweel, J. & Breugem, W.-P., 2019. Deformation of a linear viscoelastic compliant coating in a turbulent flow, *J. Fluid Mech.*, **859**, 613–658.
- Bishop, J.W., Fee, D., Modrak, R., Tape, C. & Kim, K., 2021. Spectral element modeling of acoustic to seismic coupling over topography, *J. geophys. Res.*, **127**(1), doi:10.1029/2021JB023142.
- Boiero, D., Wiarda, E. & Vermeer, P., 2013. Surface- and guided-wave inversion for near-surface modeling in land and shallow marine seismic data, *Leading Edge*, **32**(6), 638–646.
- Brinkman, N. *et al.*, 2022. In situ regolith seismic velocity measurement at the InSight landing site on Mars, *J. geophys. Res.*, **127**(10), e2022JE007229.
- Brissaud, Q., Martin, R., Garcia, R.F. & Komatitsch, D., 2017. Hybrid Galerkin numerical modelling of elastodynamics and compressible Navier-Stokes couplings: applications to seismo-gravito acoustic waves, *J. geophys. Int.*, **210**(2), 1047–1069.
- Crawford, W.C., Webb, S.C. & Hildebrand, J.A., 1991. Seafloor compliance observed by long-period pressure and displacement measurements, *J. geophys. Res.*, **96**(B10), 16 151–16 160.
- Edwards, W.N., Eaton, D.W., McCausland, P.J., ReVelle, D.O. & Brown, P.G., 2007. Calibrating infrasonic to seismic coupling using the Stardust sample return capsule shockwave: implications for seismic observations of meteors, *J. geophys. Res.*, **112**(B10), doi:10.1029/2006JB004621.
- Edwards, W.N., Eaton, D.W. & Brown, P.G., 2008. Seismic observations of meteors: coupling theory and observations, *Rev. Geophys.*, **46**(4), doi:10.1029/2007RG000253.
- Ewing, W.M., Jardetzky, W.S., Press, F. & Beiser, A., 1957. *Elastic Waves in Layered Media*, McGraw-Hills Book Co.
- Farrell, J., Wu, S.-M., Ward, K.M. & Lin, F.-C., 2018. Persistent noise signal in the FairfieldNodal three-component 5-Hz geophones, *Seismol. Res. Lett.*, **89**(5), 1609–1617.
- Garcia, R.F. *et al.*, 2020. Pressure effects on the SEIS-InSight instrument, improvement of seismic records, and characterization of long period atmospheric waves from ground displacements, *J. geophys. Res.*, **125**(7), e2019JE006278.
- Garcia, R.F. *et al.*, 2022. Newly formed craters on Mars located using seismic and acoustic wave data from InSight, *Nat. Geosci.*, **15**(10), 774–780.
- Giardini, D. *et al.*, 2020. The seismicity of Mars, *Nat. Geosci.*, **13**(3), 205–212.
- Gilbert, F., 1964. Propagation of transient leaking modes in a stratified elastic waveguide, *Rev. Geophys.*, **2**(1), 123–153.
- Hasselmann, K., 1963. A statistical analysis of the generation of microseisms, *Rev. Geophys.*, **1**(2), 177–210.
- Hyndman, R. & Spence, G., 1992. A seismic study of methane hydrate marine bottom simulating reflectors, *J. geophys. Res.*, **97**(B5), 6683–6698.
- Ichihara, M., Takeo, M., Yokoo, A., Oikawa, J. & Ohminato, T., 2012. Monitoring volcanic activity using correlation patterns between infrasound and ground motion, *Geophys. Res. Lett.*, **39**(4), doi:10.1029/2011GL050542.
- Johnson, C.W., Meng, H., Vernon, F. & Ben-Zion, Y., 2019. Characteristics of ground motion generated by wind interaction with trees, structures, and other surface obstacles, *J. geophys. Res.*, **124**(8), 8519–8539.
- Kenda, B. *et al.*, 2017. Modeling of ground deformation and shallow surface waves generated by Martian dust devils and perspectives for near-surface structure inversion, *Space Sci. Rev.*, **211**(1), 501–524.
- Kenda, B. *et al.*, 2020. Subsurface structure at the InSight landing site from compliance measurements by seismic and meteorological experiments, *J. geophys. Res.*, **125**(6), e2020JE006387.
- Khan, A. *et al.*, 2021. Upper mantle structure of Mars from InSight seismic data, *Science*, **373**(6553), 434–438.
- Knapmeyer-Endrun, B. *et al.*, 2021. Thickness and structure of the martian crust from InSight seismic data, *Science*, **373**(6553), 438–443.
- Kramer, S.L., 2002. *Geotechnical Earthquake Engineering*, Prentice Hall, Inc.
- Langston, C.A., 2004. Seismic ground motions from a Bolide shock wave, *J. geophys. Res.*, **109**(B12), doi:10.1029/2004JB003167.
- Lin, T.-L. & Langston, C.A., 2007. Infrasound from thunder: a natural seismic source, *Geophys. Res. Lett.*, **34**(14), doi:10.1029/2007GL030404.
- Lognonné, P. & Johnson, C., 2007. Planetary seismology, *Treat. Geophys.*, **10**, 69–122.
- Lognonné, P. & Mosser, B., 1993. Planetary seismology, *Surv. Geophys.*, **14**(3), 239–302.
- Lognonné, P., Clévéde, E. & Kanamori, H., 1998. Computation of seismograms and atmospheric oscillations by normal-mode summation for a spherical earth model with realistic atmosphere, *J. geophys. Int.*, **135**(2), 388–406.
- Lognonné, P., Karakostas, F., Rolland, L. & Nishikawa, Y., 2016. Modeling of atmospheric-coupled Rayleigh waves on planets with atmosphere: From Earth observation to Mars and Venus perspectives, *J. acoust. Soc. Am.*, **140**(2), 1447–1468.
- Lognonné, P. *et al.*, 2020. Constraints on the shallow elastic and anelastic structure of Mars from InSight seismic data, *Nat. Geosci.*, **13**(3), 213–220.
- Lognonné, P., Banerdt, W., Clinton, J., Garcia, R., Giardini, D., Knapmeyer-Endrun, B., Panning, M. & Pike, W., 2023. Mars seismology, *Ann. Rev. Earth planet. Sci.*, **51**(1), 643–670.
- Longuet-Higgins, M.S., 1950. A theory of the origin of microseisms, *Phil. Trans. R. Soc. Lond., A*, **243**(857), 1–35.
- Lorenz, R.D., 2021. Dust devil winds: assessing dry convective vortex intensity limits at planetary surfaces, *Icarus*, **354**, doi:10.1016/j.icarus.2020.114062.
- Lorenz, R.D., Kedar, S., Murdoch, N., Lognonné, P., Kawamura, T., Mimoun, D. & Bruce Banerdt, W., 2015. Seismometer detection of dust devil vortices by ground tilt, *Bull. seism. Soc. Am.*, **105**(6), 3015–3023.
- Martire, L., Martin, R., Brissaud, Q. & Garcia, R.F., 2022. SPECFEM2D-DG, an open source software modeling mechanical waves in coupled solid-fluid systems: the linearised Navier-Stokes approach, *J. geophys. Int.*, **228**(1), 664–697.
- Marusiak, A.G., Vance, S., Panning, M.P., Bryant, A.S., Hesse, M.A., Carnahan, E. & Journaux, B., 2022. The effects of methane Clathrates on the thermal and seismic profile of Titan's icy lithosphere, *Planet. Sci. J.*, **3**(7), 167, doi:10.3847/PSJ/ac787e.
- Mucciarelli, M., Gallipoli, M.R., Di Giacomo, D., Di Nota, F. & Nino, E., 2005. The influence of wind on measurements of seismic noise, *J. geophys. Int.*, **161**(2), 303–308.
- Murdoch, N., Mimoun, D., Garcia, R.F., Rapin, W., Kawamura, T., Lognonné, P., Banfield, D. & Banerdt, W.B., 2017. Evaluating the wind-induced mechanical noise on the InSight seismometers, *Space Sci. Rev.*, **211**, 429–455.
- Nishikawa, Y., Araya, A., Kurita, K., Kobayashi, N. & Kawamura, T., 2014. Designing a torque-less wind shield for broadband observation of marsquakes, *Planet. Space Sci.*, **104**, 288–294.
- Novoselov, A., Fuchs, F. & Bokelmann, G., 2020. Acoustic-to-seismic ground coupling: coupling efficiency and inferring near-surface properties, *J. geophys. Int.*, **223**(1), 144–160.
- Onodera, K. *et al.*, 2023. Description of Martian Convective Vortices Observed by InSight and Implications for Vertical Vortex Structure and Sub-surface Physical Properties. *J. geophys. Res.*, **128**(11), e2023JE007896.

- Petculescu, A. & Achi, P., 2012. A model for the vertical sound speed and absorption profiles in Titan's atmosphere based on Cassini-Huygens data, *J. acoust. Soc. Am.*, **131**(5), 3671–3679.
- Ritzwoller, M.H. & Levshin, A.L., 2002. Estimating shallow shear velocities with marine multicomponent seismic data, *Geophysics*, **67**(6), 1991–2004.
- Ruan, Y., Forsyth, D.W. & Bell, S.W., 2014. Marine sediment shear velocity structure from the ratio of displacement to pressure of Rayleigh waves at seafloor, *J. geophys. Res.*, **119**(8), 6357–6371.
- Schumann, K., Stipp, M., Behrmann, J.H., Klaeschen, D. & Schulte-Kortnack, D., 2014. P and S wave velocity measurements of water-rich sediments from the Nankai Trough, Japan, *J. geophys. Res.*, **119**(2), 787–805.
- Sorrells, G., Bonner, J. & Herrin, E.T., 2002. Seismic precursors to space shuttle shock fronts, *Pure appl. Geophys.*, **159**(5), 1153–1181.
- Sorrells, G.G., 1971. A preliminary investigation into the relationship between long-period seismic noise and local fluctuations in the atmospheric pressure field, *J. geophys. Int.*, **26**(1–4), 71–82.
- Sorrells, G.G., McDonald, J.A., Der, Z. & Herrin, E., 1971. Earth motion caused by local atmospheric pressure changes, *J. geophys. Int.*, **26**(1–4), 83–98.
- Stähler, S.C. *et al.*, 2021. Seismic detection of the martian core, *Science*, **373**(6553), 443–448.
- Stott, A.E. *et al.*, 2021. The site tilt and lander transfer function from the short-period seismometer of InSight on Mars, *Bull. seism. Soc. Am.*, **111**(6), 2889–2908.
- Stutzmann, É. *et al.*, 2021. The polarization of ambient noise on Mars, *J. geophys. Res.*, **126**(1), e2020JE006545.
- Tanimoto, T. & Wang, J., 2019. Theory for deriving shallow elasticity structure from colocated seismic and pressure data, *J. geophys. Res.*, **124**(6), 5811–5835.
- Umlauf, J. & Korn, M., 2019. 3-D fluid channel location from noise tremors using matched field processing, *J. geophys. Int.*, **219**(3), 1550–1561.
- Webb, S.C., 1998. Broadband seismology and noise under the ocean, *Rev. Geophys.*, **36**(1), 105–142.
- Webb, S.C. & Crawford, W.C., 2010. Shallow-water broadband OBS seismology, *Bull. seism. Soc. Am.*, **100**(4), 1770–1778.
- Withers, M.M., Aster, R.C., Young, C.J. & Chael, E.P., 1996. High-frequency analysis of seismic background noise as a function of wind speed and shallow depth, *Bull. seism. Soc. Am.*, **86**(5), 1507–1515.
- Xu, Z., Mikesell, T.D., Umlauf, J. & Gribler, G., 2020. Rayleigh-wave multicomponent crosscorrelation-based source strength distribution inversions. Part 2: a workflow for field seismic data, *J. geophys. Int.*, **222**(3), 2084–2101.
- Xu, Z., Froment, M., Garcia, R.F., Beucler, É., Onodera, K., Kawamura, T., Lognonné, P. & Banerdt, W.B., 2022. Modelling seismic recordings of high-frequency guided infrasound on Mars, *J. geophys. Res.*, **127**(11), e2022JE007483.
- Yamamoto, T. & Torii, T., 1986. Seabed shear modulus profile inversion using surface gravity (water) wave-induced bottom motion, *J. geophys. Int.*, **85**(2), 413–431.
- Yu, J., Raspet, R., Webster, J. & Abbott, J., 2011. Wind noise measured at the ground surface, *J. acoust. Soc. Am.*, **129**(2), 622–632.
- Zhang, L., Gao, F., Liu, Z., Cao, P. & Zhang, J., 2022. Temperature-dependent modal analysis of InSight lander on Mars, *Geophysics*, **88**(2), 1–21.

APPENDIX A: ACOUSTIC-WAVE INCIDENCE AND HOMOGENEOUS-MEDIUM COMPLIANCE

We consider a special case of compliance, an acoustic wave propagating towards the flat free surface of a homogeneous elastic medium. We write this incident acoustic wave as $p = P_0 \exp \left[i\omega(t - \frac{\sin\theta}{V_a}x - \frac{\cos\theta}{V_a}z) \right]$, where V_a is the acoustic-wave speed and θ is the incident angle (Fig. A1). This incidence wave is

reflected on the solid medium surface, and we write the reflected acoustic wave as $p_1 = P_1 \exp \left[i\omega(t - \frac{\sin\theta}{V_a}x + \frac{\cos\theta}{V_a}z) \right]$. The atmospheric pressure on the surface ($z = 0$) due to the incident and reflected acoustic waves is $(P_0 + P_1) \exp \left[i\omega(t - \frac{\sin\theta}{V_a}x) \right]$. Here we ignore the atmospheric winds.

For this incident acoustic wave, the particle velocities on the surface are written as

$$v_z(z = 0) = \frac{-\partial_z p}{i\omega\rho_0} = \frac{\cos\theta P_0}{\rho_0 V_a}, \quad (\text{A1})$$

$$v_x(z = 0) = \frac{-\partial_x p}{i\omega\rho_0} = \frac{\sin\theta P_0}{\rho_0 V_a}, \quad (\text{A2})$$

where ρ_0 is the air density, and we omit $\exp \left[i\omega(t - \frac{\sin\theta}{V_a}x) \right]$ for brevity. Note that the particle motion above is identical to a P -wave incidence with the velocity amplitude $\frac{P_0}{\rho_0 V_a}$. We refer to this P wave as the equivalent P wave in the following.

This incident acoustic wave generates the transmitted P and Sv waves in the medium. Combing the P - Sv -wave reflection and transmission (e.g. Aki & Richards 2002) with the equivalent P wave, we compute the transmission coefficients (T_{PP} and T_{PS}) of the transmitted P and S waves, respectively. The angles for these two waves are θ_P and θ_S . We also compute the P -wave reflection coefficient, which is equal to the amplitude ratio between the incident and reflected acoustic waves, P_1/P_0 .

Finally, the compliance due to this acoustic-wave incidence is written as as:

$$C_Z(z_0) = \frac{P_0(T_{PP} \cos\theta_P - T_{PS} \sin\theta_S)}{\rho_0 V_a (P_0 + P_1)}, \quad (\text{A3})$$

$$C_H(z_0) = \frac{P_0(T_{PP} \sin\theta_P + T_{PS} \cos\theta_S)}{\rho_0 V_a (P_0 + P_1)}. \quad (\text{A4})$$

The compliance values from these two formulas match well with the values from our theory, eqs (5) and (6) (Fig. 2).

The energy ratio between the reflected and the incident acoustic waves is $R_{PP}^2 = (P_1/P_0)^2$ (e.g. Aki & Richards 2002; Lognonné & Johnson 2007). Consequently, the energy ratio of the transmitted body waves, that is the percentage of the energy converted into the solid, is $1 - R_{PP}^2$.

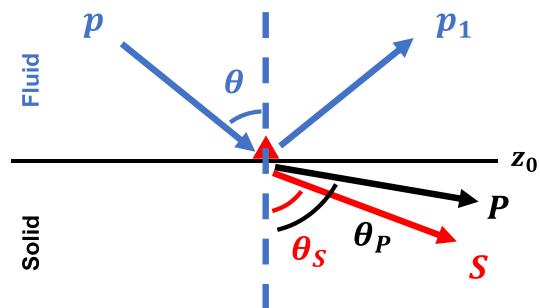


Figure A1. Illustration of acoustic wave interacting with the underlying solid medium. The blue arrows represent incident and reflected acoustic waves. The red and black arrows are the transmitted P and S waves in the solid, respectively.

APPENDIX B: HOMOGENEOUS-MEDIUM COMPLIANCE AND SORRELLS'S THEORY

For a low-speed horizontal-propagating fluid pressure perturbation like winds, we assume $c \ll \beta$ and thus rewrite γ and ν (Section 2) as:

$$\gamma = \frac{\omega}{c} \sqrt{1 - \frac{c^2}{\alpha^2}} \approx \frac{\omega}{c} \left(1 - \frac{1}{2} \frac{c^2}{\alpha^2}\right), \quad (\text{B1})$$

$$\nu = \frac{\omega}{c} \sqrt{1 - \frac{c^2}{\beta^2}} \approx \frac{\omega}{c} \left(1 - \frac{1}{2} \frac{c^2}{\beta^2}\right). \quad (\text{B2})$$

By plugging these two formulas into the compliance equations (eqs 5 and 6) and neglecting the second-order term like $(c/\beta)^2$, we recognize that the compliance equations become:

$$C_Z(z_0) = -\frac{ic\alpha^2(1 - c^2/\alpha^2)}{2\mu(\alpha^2 - \beta^2)} \approx -\frac{ic(\lambda + 2\mu)}{2\mu(\lambda + \mu)}, \quad (\text{B3})$$

$$C_H(z_0) = -\frac{c\beta^2}{2\mu(\alpha^2 - \beta^2)} = -\frac{c}{2(\lambda + \mu)}, \quad (\text{B4})$$

where the third part of each equation above is identical to Sorrells (1971).

APPENDIX C: BENCHMARK OF COMPUTING COMPLIANCE AT DEPTH

We benchmark our computation against SPEC-FEM2D-DG (Brisaud *et al.* 2017; Martire *et al.* 2022), a numerical simulation software designed for modelling wave propagation in a mechanically coupled solid–fluid system. In our utilizing this software, the over-

lying fluid is a homogeneous atmosphere with an acoustic-wave velocity of 340 m s^{-1} . We set the underlying solid medium to be homogeneous, where $\alpha = 2003 \text{ m s}^{-1}$, $\beta = 1200 \text{ m s}^{-1}$ and $\rho = 2074 \text{ kg m}^{-3}$. We impose an atmospheric pressure source at 5 m above the solid medium surface, where 5 m is the grid spacing. This source emits a Gaussian wavelet with a centre frequency of 15 Hz. We position receivers vertically, and place them 500 m horizontally away from the source. One of the receivers, located in the atmosphere 5 m above the surface, records the atmospheric pressure. All other receivers are in the solid medium and record both horizontal and vertical particle velocities at different depths, from the surface to 50 m depth. From these recordings, we extract the data following the seismic arrivals generated by the source to compute the compliance values (Fig. C1).

In this simulation setting, the acoustic wave from the source propagates almost horizontally along the solid medium surface. The compliance values from our theoretical computation agrees well with the ones from SPEC-FEM2D-DG, especially when the receiver depth is less than 10 m (Fig. C1). However, when the receiver depth is larger than 10 m, the theoretical and SPEC-FEM2D-DG compliance values start to diverge at certain frequencies (such as 15 Hz at 20 m depth and 6 Hz at 50 m depth). This divergence occurs because with increasing depth, the compliance amplitude decreases (Section 4) and thus particle motions at a given frequency become more influenced by other factors in the simulation like numerical noise. Furthermore, the frequency where this divergence occurs decreases with increasing depth. This is due to that compliance amplitudes at lower frequencies decay slower with depth, leading to at a given depth, the compliance results from SPEC-FEM2D-DG at lower frequencies are less affected by numerical noise compared to at higher frequencies (Figs 4 and S2).

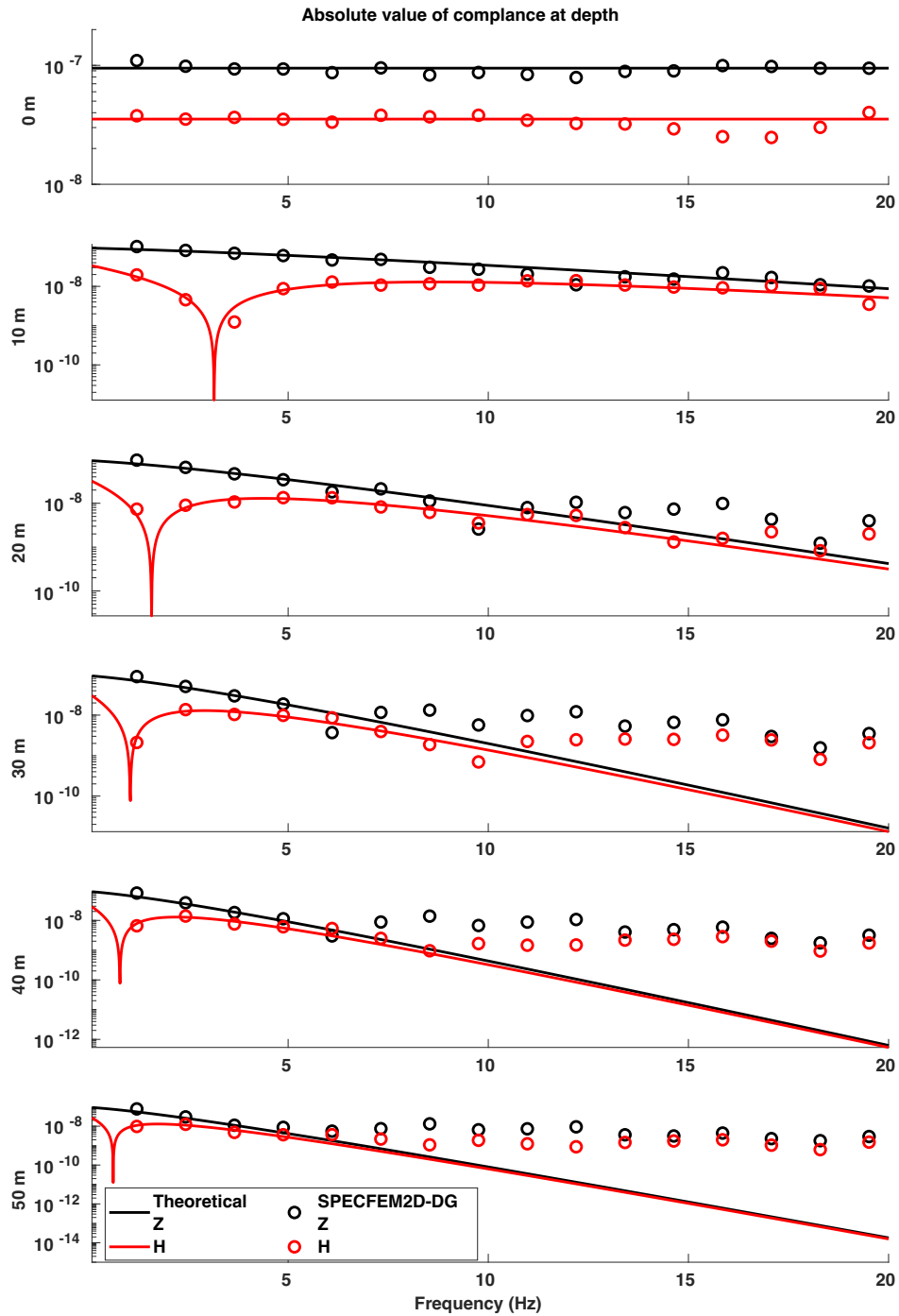


Figure C1. Comparison of the vertical and horizontal compliance values at different depth from our theory (Section 4) and SPECFEM2D-DG.